Ultrahigh critical current densities, the vortex phase diagram, and the effect of granularity of the stoichiometric high-T_c superconductor $CaKFe_4As_4$

Shiv J. Singh,[1] Matthew Bristow,[1] William R. Meier,[2,3] Patrick Taylor,[1] Stephen J. Blundell,[1] Paul C. Canfield,[2,3] and Amalia I. Coldea[1]

[1]*Clarendon Laboratory, Department of Physics, University of Oxford, Parks Road, Oxford OX1 3PU, United Kingdom*

[2]*Ames Laboratory, Iowa State University, Ames, Iowa 50011, USA*

[3]*Department of Physics and Astronomy, Iowa State University, Ames, Iowa 50011, USA*

(Received 9 May 2018; published 30 July 2018)

We present a comprehensive study of the critical current densities and the superconducting vortex phase diagram in the stoichiometric superconductor $CaKFe_4As_4$ which has a critical temperature of ~35 K. We performed detailed magnetization measurements both of high quality single crystals for different orientations in an applied magnetic field up to 16 T and for a powder sample. We find an extremely large critical current density, J_c, up to 10^8 A/cm^2 for single crystals when $H\|(ab)$ at 5 K, which remains robust in fields up to 16 T, being the largest of any other iron-based superconductor. The critical current density is reduced by a factor 10 in single crystals when $H\|c$ at 5 K and significantly suppressed by the presence of grain boundaries in the powder sample. We also observe the presence of the fishtail effect in the magnetic hysteresis loops of single crystals when $H\|c$. The flux pinning force density and the pinning parameters suggest that the large critical current could be linked to the existence of point core and surface pinning. Based on the vortex phase diagram and the large critical current densities, $CaKFe_4As_4$ is now established as a potential iron-based superconductor candidate for practical applications.

DOI: 10.1103/PhysRevMaterials.2.074802

I. INTRODUCTION

The discovery of iron based superconductors [1,2] has led to important advances in superconductivity not only because of their unconventional superconducting mechanism with rather high superconducting transition temperatures, but also due to their potential for high magnetic field applications, such as superconducting wires and tapes. The bulk iron-based superconductors have a high transition temperature of up to 58 K [3,4] and very high upper critical field (H_{c2}) up to 100 T [5,6]. Furthermore, their high upper critical field, small anisotropy, good grain boundary connectivity, and high critical current density under high magnetic field are all important factors contributing to their suitability for practical applications [7,8].

Among iron-based superconductors, the recently discovered $CaKFe_4As_4$ is a member of a new 1144 structural family of iron-based superconductors, being a stoichiometric optimally-doped superconductor, with a transition temperature, T_c, around 35 K and large upper critical field up to 90 T [9,10]. A number of transport, thermal, and thermodynamics experiments on $CaKFe_4As_4$ do not show any structural transition or magnetic order [9,10]. This system displays similar superconducting properties to those of the optimally-doped $Ba_{1-x}K_xFe_2As_2$ (BaK122) system [11]. $CaKFe_4As_4$ has a tetragonal structure ($P4/mmm$), where Ca and K layers stack alternatively across the Fe_2As_2 layer along the c axis [9,10]; Fe-As bond distances are different for the As atoms above and below the Fe plane, in contrast to the 122 system that has equivalent Fe-As distances. The lowering in symmetry has significant consequences on the electronic structure of $CaKFe_4As_4$, being that of a compensated metal with a large number of electronic bands close to a nesting instability [12] as well as on its magnetic structure which forms an unusual spin-vortex crystal order by Ni or Co doping [13].

Generally, iron-based superconductors possess a layered structure similar to that of the high-T_c cuprates. Superconductivity in these systems often appears out of an antiferromagnetic state with bad metallic behavior, found in the parent compounds, which is suppressed by electron (or hole) doping [2,14,15] or by application of external pressure [2], giving rise to complex superconducting phase diagrams [2,14,15]. The understanding of the superconducting mechanism of unconventional superconductors is challenging due to different competing electronic phases, but the existence of few stoichiometric iron-based superconductors provides a unique opportunity to study this phenomenon in the absence of additional extrinsic effects introduced by chemical substitutions.

The critical current density, J_c, is an essential property of the high-T_c superconductors in order to identify the best candidates for practical applications. A high J_c exceeding 10^5 A/cm^2 even under high magnetic field above 10 T is found in many optimally-doped iron-based superconductors [7]. The high transition temperatures, large magnetic penetration depth, vortex motion, and thermal fluctuation generally plays an important role in the critical current properties, similar to the high-T_c cuprates. These phenomena cause interesting effects in the vortex dynamics, such as giant-flux creep, thermally activated flux flow, and the presence of a second magnetization peak or the fish-tail effect [16,17]. The ability to carry the critical current is governed by the vortex pinning strength and motion. Different kinds of pinning determine the elastic or plastic motion of vortex lattice, formation of vortex glass,

 ©2018 American Physical Society

vortex melting, and order-disorder phase transitions [17,18]. As vortex motion is strongly affected by disorder in superconductors, it is important to understand what happens in a stoichiometric and clean high-T_c superconductor, such as $CaKFe_4As_4$.

In the present study, we report the superconducting properties and the critical current densities of $CaKFe_4As_4$ in both single crystals and polycrystalline samples using magnetization measurements in magnetic fields up to 16 T. We find that $CaKFe_4As_4$ exhibits an ultrahigh critical current density of $J_c \sim 10^8$ A/cm^2 at 5 K, when the magnetic field is parallel with the conducting plane, as extracted from isothermal magnetic hysteresis loops. Critical current density is reduced by a factor 10 in single crystals, when the magnetic field is parallel with the c axis at 5 K, and it is significantly suppressed by the effect of grain boundaries in powder samples. Our study compares the behavior of the lower critical field (H_{c1}) and the upper critical field (H_{c2}) of single crystals and the vortex phase diagram of single and polycrystalline samples. We detect the presence of a second magnetization peak in the magnetic hysteresis loops of single crystals when $H \| c$. The flux pinning force density and the pinning parameters suggest the existence of surface and point core pinning of vortices. Our results suggest that $CaKFe_4As_4$, with such large critical current densities and very high upper critical fields, is an exciting new candidate for practical applications.

II. EXPERIMENTAL DETAILS

The single crystal $CaKFe_4As_4$ samples were grown by the FeAs self-flux method and polycrystalline sample were synthesized by solid state reaction method, as detailed elsewhere [9,10,19]. The single crystals have rectangular shapes for both magnetic and resistivity measurements, whereas the polycrystalline sample was pressed powder in a cylindrical shape. Magnetic measurements were carried out using the VSM (vibrating sample magnetometer) option of a physical property measurement system (PPMS-Quantum Design) with the magnetic fields up to 16 T. The magnetic isotherms were recorded up to 16 T with a ramping rate of 3 mT/s, at several temperatures ranging from 2 up to 40 K. All the hysteresis loops at constant temperatures, $M(H)$, and temperature dependent magnetization in constant magnetic field, $M(T)$, were performed after cooling the sample in zero magnetic field from above T_c.

Magnetization hysteresis loops allow us to extract the critical current density, J_c, as a function of magnetic field using the extended Bean's critical state model [20]. The vortex pinning force density can be estimated using $F_P = J_c \times \mu_0 H$ [21]. For a rectangular crystal, the magnetic field dependence of the critical current density, J_c (in units of A/cm^2) is given by the relation $J_c = 2\Delta M/[a_s(1 - a_s/3b_s)]$ (for $a_s < b_s$); $\Delta M = M_{up} - M_{dn}$, and M_{up} and M_{dn} are the magnetization while magnetic fields are decreasing and increasing, respectively. The magnetization ΔM expressed in A/cm is obtained from the magnetic moment divided by the sample volume, $V = a_s \times b_s \times c_s$, where a_s and b_s are in-plane sample dimensions perpendicular to the applied magnetic field and c_s is the sample dimension parallel to the applied magnetic field. We have measured a single crystal of $CaKFe_4As_4$ with the following dimensions: $a_s = 1.09$ mm, $b_s = 1.365$ mm, and $c_s = 0.0025$ mm, measured with the magnetic field aligned along the c axis ($H \| c$) and $a_s = 0.0025$ mm, $b_s = 1.09$ mm, and $c_s = 1.365$ mm, measured with the magnetic field aligned in the ab plane ($H \| (ab)$). The sample thickness of the crystal was evaluated using Gaussian fits to the different optical image measurements across the sample, as shown in Fig. 7. For the cylindrical pressed powder sample in order to estimate the critical current, J_c, we used the expression $J_c = 3\ \Delta M/d$, where $d = 5.03$ mm and $l = 4.08$ mm are the diameter and length of the cylinder, respectively [20]. The average grain size for the powder sample is around 1.7(7) μm.

To estimate the lower critical field, H_{c1}, M (H) loops were measured up to 0.5 T sweeping the field with a slow rate of 0.2 mT/s at each temperature. Before each measurement the sample was warmed up above T_c, and the remnant field of the magnet is reduced before cooling down to the target temperature. The susceptibility data $\chi = M/H$ has been corrected for the demagnetization effect [22]. For an applied external field H_a, the internal field $H_i = H_a - N_{\text{eff}} M$, where N_{eff} is the effective demagnetization factor. For the accurate determination of H_{c1}, we subtracted the value of magnetization obtained by the low-field magnetization slope from the magnetization (M) for each isotherm [23]. The deviation point of magnetization versus field from linear behavior gives the value of the first penetration field, H^*_{c1}. We estimate the effective demagnetization factor for our single crystal to be $N_{\text{eff}} = 0.995$ when $H \| c$, which is similar to the calculated demagnetization factor for this orientation [22]. When $H \| (ab)$ the value of $N_{\text{eff}} = 0.70$ which is extracted from zero-field cooled data assuming that in the orientation the sample is a perfect diamagnet as for $H \| c$. $N_{\text{eff}} = 0.41$ for the cylindrical polycrystalline sample is extracted both from calculations and experiment [22,24]. The upper critical field, H_{c2}, is extracted from the temperature dependence of magnetization at different constant magnetic field up to 16 T.

III. RESULTS AND DISCUSSION

The temperature dependence of the magnetic susceptibility (χ) from zero-field-cooled (ZFC) and field-cooled (FC) magnetization measurements in low magnetic field (2 or 5 mT) for single crystal (when $H \| c$ and $H \| (ab)$) and for the powder sample of $CaKFe_4As_4$ are shown in Figs. 1(a)–1(c). A perfect diamagnetic state is reached at low temperatures for all measured samples. The critical temperature T_c is defined around 35 K from the bifurcation point between ZFC and FC branches of the magnetization in Fig. 1. The width of the superconducting transition is very narrow for the single crystal ($\Delta T_c \sim 1$ K) suggesting a high quality of this sample, as shown by the x-ray and resistivity data in the Appendix in Fig. 7. The powder sample also shows perfect diamagnetism at low temperatures but it has a much broader transition of ($\Delta T_c \sim 12$ K), likely due to pinning to grain boundaries and grain size effects, as seen in other iron-based superconductors [25]. No secondary phases were identified in our powder sample, as shown in Fig. 8. The small diamagnetic signal in the FC data reflects the strong pinning nature of the sample and permanent flux trapped inside it.

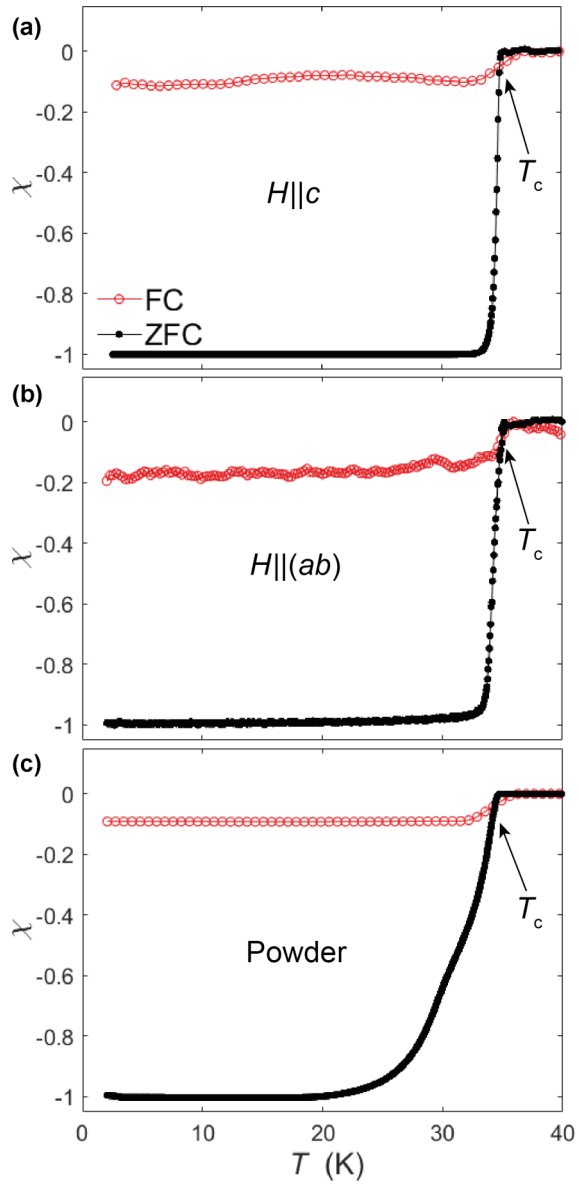

FIG. 1. Temperature dependence of magnetic susceptibility (χ) deduced from zero-field cooled and field-cooled magnetization measurements for single crystal when (a) $H \| c$ and (b) $H \| (ab)$ in 5 mT as well as (c) the powder sample in 2 mT. The arrows indicate the positions of the onset values of the critical temperature T_c.

The temperature dependence of the superconducting lower critical field, H_{c1}, is determined using low-field magnetic hysteresis measurements, as shown in Figs. 2(a)–2(c). We measured the field dependence of the magnetization in the superconducting state at different temperatures, with the external field in the (ab) plane and along the c axis and also for the powder sample. The linear variation of the magnetization is a signature of the Meissner state up to H_{c1}, above which the vortices starts to form. The temperature dependence of the extracted H_{c1} for the single crystal and the powder sample is shown in Fig. 2(d). The values of H_{c1} for $H \| (ab)$ is higher than that for $H \| c$. The H_{c1} value for polycrystalline sample lies in between these two orientations of the single crystal [as shown in Fig. 2(d)], as expected from the powder averaging effects, and it was extracted by fitting a linear dependence to the magnetization above the anomaly caused by the grain boundaries. The $H_{c1}(T)$ powder data show a very weak temperature dependence at low temperatures below 10 K, consistent with recent μSR results [26].

To determine the upper critical field, H_{c2}, we have measured zero-field-cooled magnetization in the temperature range between 2 to 40 K for various values of the magnetic field up to 16 T, shown in Figs. 2(f)–2(h) for the single crystal and the powder sample, respectively. The upper critical field, $H_{c2}(T)$, as a function of temperature near T_c is defined by the value at which magnetization starts to deviate from the high-temperature paramagnetic value. Just below the critical temperature, we noticed a small jump in the temperature dependence of zero-field magnetization for both the single crystal and the powder sample, being more pronounced as the field increases. This effect may be caused by the flux jumps.

Figure 2(i) shows the H-T phase diagram of $CaKFe_4As_4$ calculated from magnetization data. Since the transition temperature is not significantly suppressed with magnetic field, it indicates a very high value of $H_{c2}(0)$. To estimate $H_{c2}(0)$ we use the Werthamer-Helfand-Hohenberg (WHH) formula [27] close to T_c, $\mu_0 H_{c2}(0) = -0.69 T_c (\mu_0 \mathrm{d}H_{c2}/\mathrm{d}T)$. The slope of upper critical field $(-\mu_0 \mathrm{d}H_{c2}/\mathrm{d}T)$ (see Table I) ranges between 2.6(1) for $H \| c$, to 5.7(7) for $H \| (ab)$ for the single crystal and 10.1(5) $\mathrm{T}K^{-1}$ for the powder sample. Using the transition temperature as $T_c = 35$ K, we find $\mu_0 H_{c2}$ at zero temperature of ~62 T when $H \| c$ and a much larger value of 135 T when $H \| (ab)$. The powder sample show a significantly larger upper critical field of 241 T, a factor of ~4 larger than in single crystals. We have also measured the resistivity for a different single crystal, as shown in Fig. 7(c). The slope of upper critical field from transport data measured in magnetic field (not shown here [28]) gives much larger upper critical fields, $\mu_0 H_{c2}(0) = 82$ T, and 168 T for $H \| c$ and $H \| (ab)$, respectively, similar to those reported previously [10].

Using the zero temperature value of upper critical field $H_{c2}(0)$, the corresponding value of $\mu_0 H_{c2}(0)/k_B T_c$ is close to 1.8 for $H \| c$, and increases to 3.9 when $H \| (ab)$ and 6.9 $\mathrm{T\,K^{-1}}$ for the powder sample. The Pauli limit is reached when the condensation energy is overcome by the Zeeman energy for normal electrons, defined as $\mu_0 H_p / T_c = 1.84\ \mathrm{T\,K^{-1}}$ in the case of singlet pairing and weak spin-orbit coupling [29,30]. In order to estimate the superconducting order parameter we used the Ginzburg-Landau (GL) approach. This gives a coherence length extrapolated to zero temperature as $\xi_{ab} = 1.9$ nm, $\xi_c = 0.87$ nm for the single crystal [as shown in Fig. 2(j)] and $\xi = 0.97$ nm for the powder sample. The extracted mean free path is $\ell = 15.7$ nm (using carrier concentration reported in Ref. [10]) based on the extrapolated normal resistivity at zero temperature of $\rho_n \sim 15.9\ \mu\Omega$ cm [see Fig. 7(c)]. This suggests that our crystals lie within the clean limit with $\xi(0) \ll \ell$ as also found in Ref. [10].

The H_{c1} values extracted in Fig. 2(d) were used to calculate the London penetration depth as a function of temperature, $\lambda(T)$. In order to estimate the penetration depth for the powder sample, we correct the value for demagnetizing effects (as detailed earlier using $N_{\mathrm{eff}} = 0.41$) and estimate the value of the Ginzburg-Landau parameter as $\kappa \sim 88$. This gives a low temperature London penetration depth $\lambda(0)$ of 104 nm [as

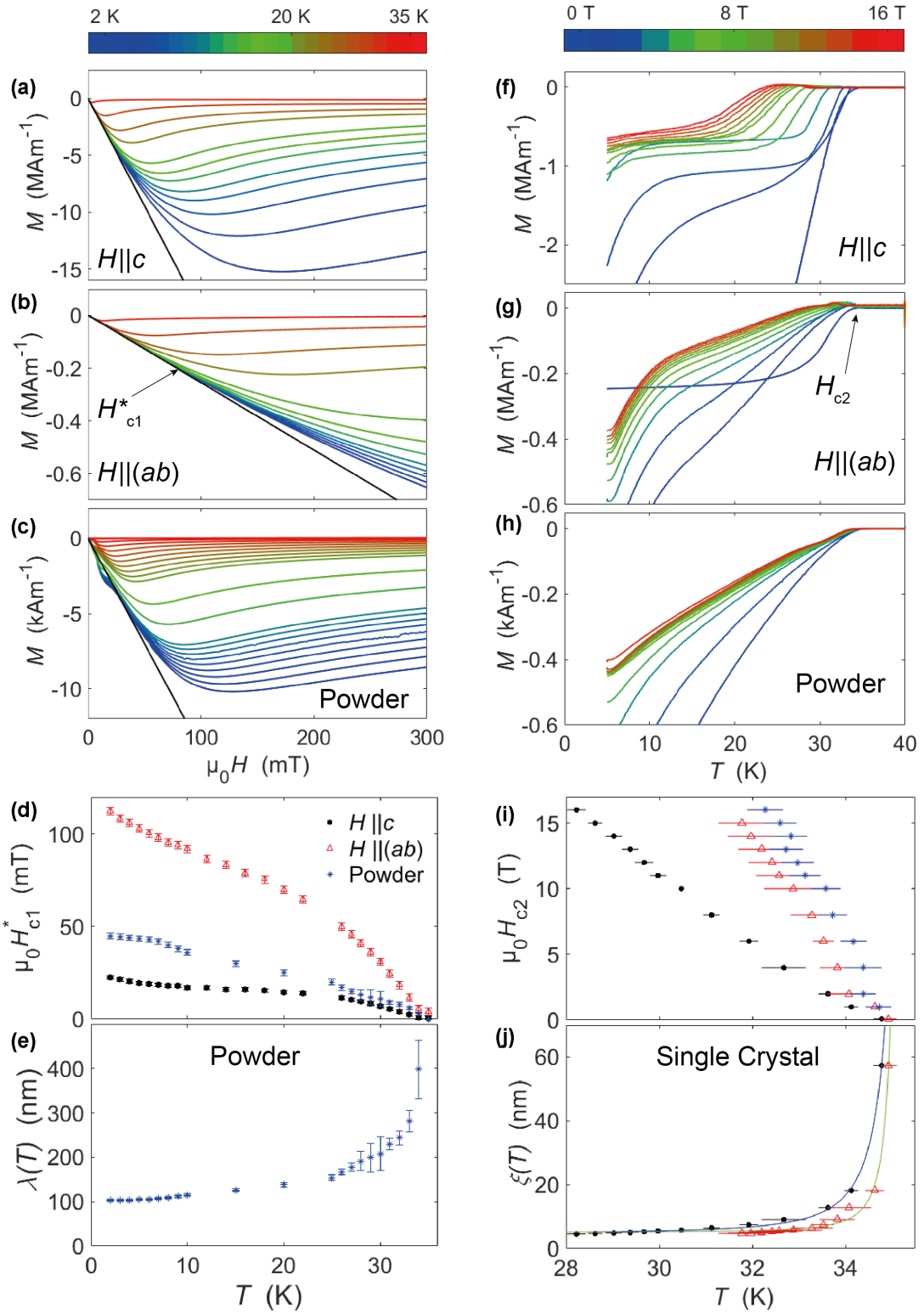

FIG. 2. Magnetization M versus magnetic field at constant temperatures for the single crystal when (a) $H \| c$ and (b) $H \| (ab)$ as well as for (c) the powder sample of $CaKFe_4As_4$. The arrow in (b) shows the point of deviation of magnetization from linear dependence in the Meissner state, defined as the first penetration field H^*_{c1}. (d) The temperature dependence of the lower critical field H^*_{c1} measured for the single crystal in two orientations in magnetic field as well as the powder sample. (e) The penetration depth λ for the powder sample. The temperature dependence of magnetization in different magnetic fields up to 16 T for the single crystal in two orientations in (f) and (g) and for the powder sample in (h). (i) The upper critical field H_{c2} versus temperature for the single crystal and the powder sample. (j) The coherence lengths, ξ_{ab} and ξ_c, for a single crystal of $CaKFe_4As_4$.

shown in Fig. 2(e)], which is similar to the value of 133 nm, extracted from London penetration depth studies in single crystals [31]. Muon relaxation studies estimate the penetration depth as 209 nm for a single crystal [32] and 286 nm for a powder sample [26].

Figures 3(a)–3(c) show the $M(H)$ loops at constant temperatures between 2 to 35 K in a magnetic field up to 16 T for the single crystal in the two orientations ($H\|(ab)$ and $H\|c$) and for the powder sample, respectively. The hysteresis areas decreased with increasing temperature and the symmetrical shape of $M(H)$ loops imply the existence of flux pinning centers. This suggests that the magnetization is dominated by bulk pinning rather than surface and geometrical barriers [21]. Furthermore, the magnetic hysteresis loop in Figs. 3(b) when $H\|(ab)$ displays a dip near zero magnetic field which may be caused by the highly inhomogeneous field distribution in the vortex state [41] and the anisotropy of J_c [42].

The second magnetization peak (SMP) can be easily seen for the single crystal below 26 K when $H\|c$, as shown in Fig. 3(a). With decreasing temperature, the peak moves to higher magnetic fields beyond the maximum applied magnetic field of 16 T. In the region between the valley and the peak, the width of the irreversible magnetization, ΔM, in Fig. 3(a) extends with increasing magnetic field and shows a clear fishtail effect. This effect was observed in other superconducting single crystals, such as cuprates [43,44], Nb_3Sn [45], MgB_2 [46] and iron-based superconductors, such as BaK122 [34] and LiFeAs [36]. Although its origin is not fully explained, the fishtail effect is strongly dependent on the sample orientation in externally applied magnetic field, being diminished when $H\|(ab)$. Importantly, the width of the $M(H)$ loops for $H\|(ab)$ [Fig. 3(b)] is much larger than of the loops for $H\|c$ [Fig. 3(a)] or the powder sample [Fig. 3(c)], implying that the pinning mechanisms are anisotropic and strongly affected by the granularity. Similar effects caused by anisotropy of flux pinning were observed in other iron-based superconductors, such as Fe(Se,Te) [35] and SmFeAs(O,F) [33].

According to the extended Bean model [20], the critical current density (J_c) can be determined from the hysteresis loop height (ΔM). As the critical current remains rather constant with the change of magnetic field for the low temperature magnetization isotherms, the extended Bean's model gives a good estimation of the critical current density in our case. Other models that take into account the field variation of the

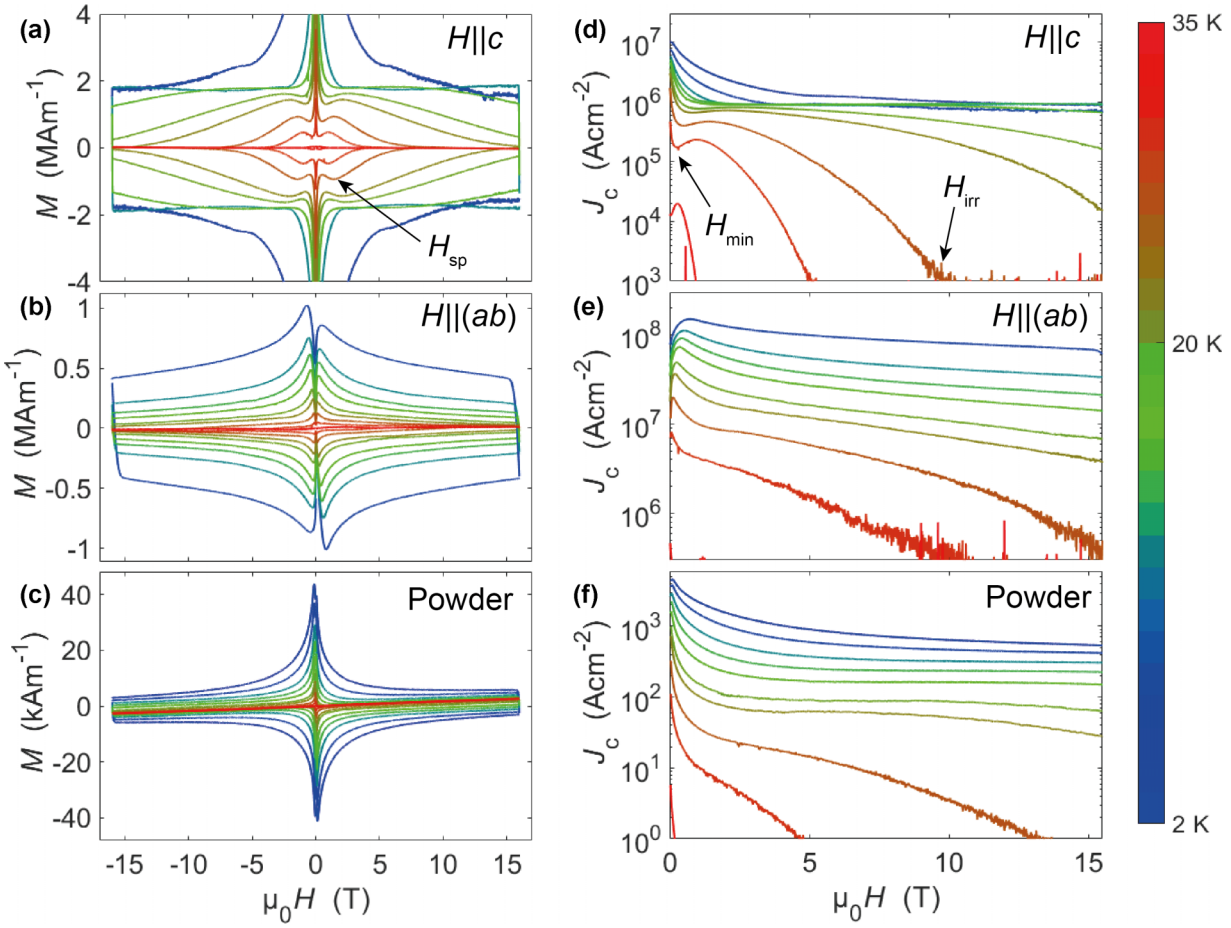

FIG. 3. The isothermal magnetization loops, $M(H)$, for the single crystal in two orientations with (a) $H\|c$ and (b) $H\|(ab)$ and (c) the powder sample of $CaKFe_4As_4$. The critical current density J_c calculated from $M(H)$ using the Bean model [20], plotted as a function of magnetic field at constant temperatures for the single crystal (d) when $H\|c$ and (e) $H\|(ab)$ and (f) the powder sample, respectively. The arrows indicate the positions of H_{sp} in (a) and H_{irr} and H_{min} in (d).

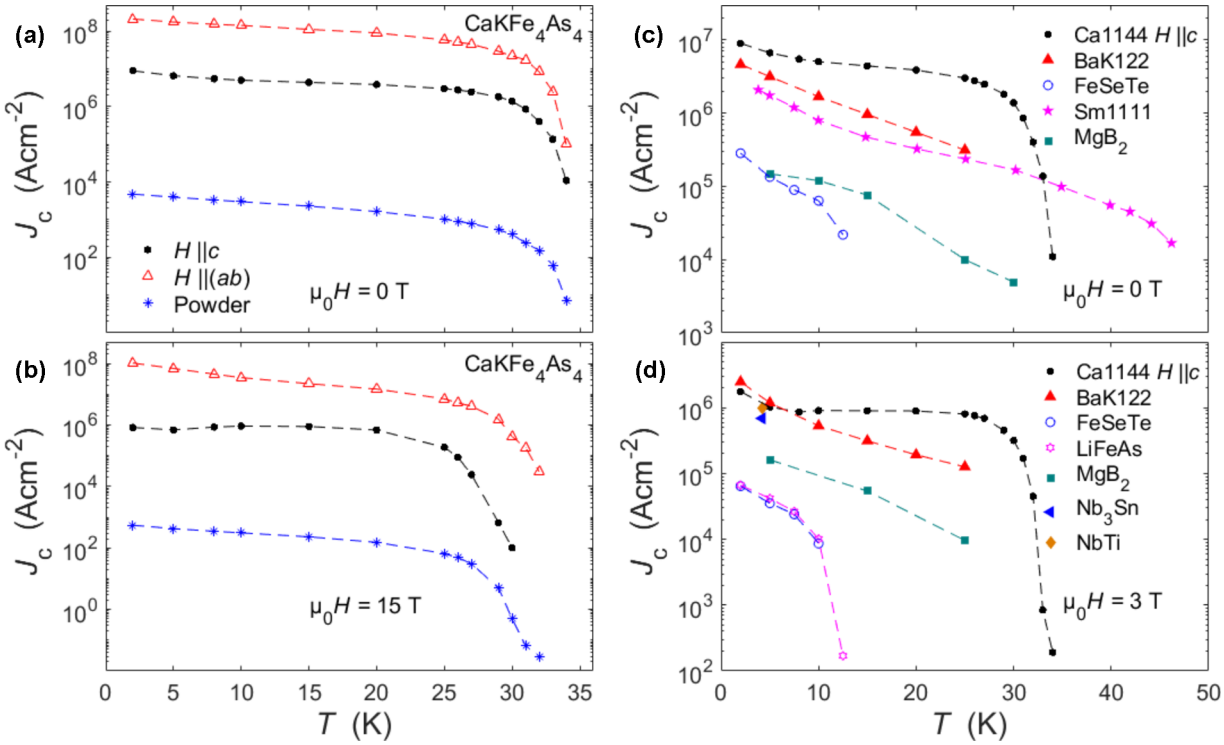

FIG. 4. The temperature dependence of critical current density J_c extrapolated at (a) $\mu_0 H = 0$ T and (b) $\mu_0 H = 15$ T of the single crystal in the two orientations in magnetic field and of the powder sample of $CaKFe_4As_4$. Comparison between the temperature dependence of the critical current density J_c (calculated using the Bean model [20]) in single crystals of $CaKFe_4As_4$ with those reported for different iron-based superconductors (SmFeAs(O,F) [33], $(Ba,K)Fe_2As_2$ [34], Fe(Se,Te) [35], LiFeAs [36]) and conventional superconductors (MgB_2 [37–39], Nb_3Sn [39], NbTi [40]) in a magnetic field of (c) 0 T and (d) 3 T for $H||c$.

critical current density and the vortex dynamics were also developed by Kim in Ref. [47] and Kim-Anderson and in Ref. [48]. Figures 3(d)–3(f) show the field dependence of J_c at constant temperatures obtained for the single crystal for different orientations in magnetic field and for the powder sample, respectively. The value of J_c for $H\|(ab)$ has ultrahigh values of the order of 10^8 A/cm^2, which is an order of magnitude larger than the value obtained when $H\|c$. However, the powder sample has a J_c which is at least three orders of magnitude lower than that of the single crystal (Table I), but similar to other polycrystalline iron-based superconductors [7,8]. The low value of J_c of the powder sample is not surprising because the magnetic behavior is significantly affected by the extrinsic factors, such as grain morphology, surface roughness, intergrain voids, and interfaces [7]. These extrinsic factors could be reduced by improving the synthesis process by adopting a ball-milling process, resintering, and the optimization of both the temperature and length of the preparation process.

Figures 3(d) and 3(e) show that J_c of $CaKFe_4As_4$ is robust and little affected by a magnetic field up to 16 T, reaching a value of $\sim 1.9(2) \times 10^8$ A/cm^2 for $H\|(ab)$ for 1 T and only dropping to $\sim 0.7(2) \times 10^8$ A/cm^2 by 15 T. These are some of the highest values obtained for any iron-based superconductor single crystal. This critical current value suggests strong vortex pinning, establishing this stoichiometric high-T_c compound as a potential candidate for practical applications. To further emphasise this important aspect, we have plotted J_c value for single crystal and the powder sample with respect to temperature for different magnetic fields of 0 and 15 T, as shown in Figs. 4(a) and 4(b), respectively. We find that J_c remains large over a large temperature range between 2 to 25 K, even with increasing magnetic field up to 15 T. Furthermore, when comparing the temperature dependence of its critical current (for $H||c$ at 0 T and 3 T) with other single crystals of iron-based superconductors or conventional superconductors in Figs. 4(c) and 4(d), it is evident that $CaKFe_4As_4$ displays an ultrahigh self-field J_c around 10^7 A/cm^2 for $H||c$ and these characteristics remain robust up to 31 K in 3 T (up to a value of 10^6 A/cm^2). To further confirm these large J_c values, we have measured additional crystals, as shown in Fig. 9 and Table I that show very similar values to those presented earlier; a slight decrease in J_c is noticed as the thickness of the sample increases from 2 μm towards 15 μm (see Table I). These high J_c values of this stoichiometric clean superconductor with a relatively low residual resistivity ($\rho_0 \sim 15.9$ $\mu\Omega$ cm) and close to an optimum doping is surprising, as one would expect a high density of defects to achieve effective pinning and large critical currents.

In order to understand the nature of pinning, we study the temperature and field dependencies of vortex pinning force density, F_P, given by $F_P = \mu_0 H \times J_c$, when $H \perp J_c$. According to the Dew-Hughes model [21], if a dominant vortex pinning mechanism exists in a certain temperature range, the normalized vortex pinning force density $f_P = F_P / F_P^{\max}$ at

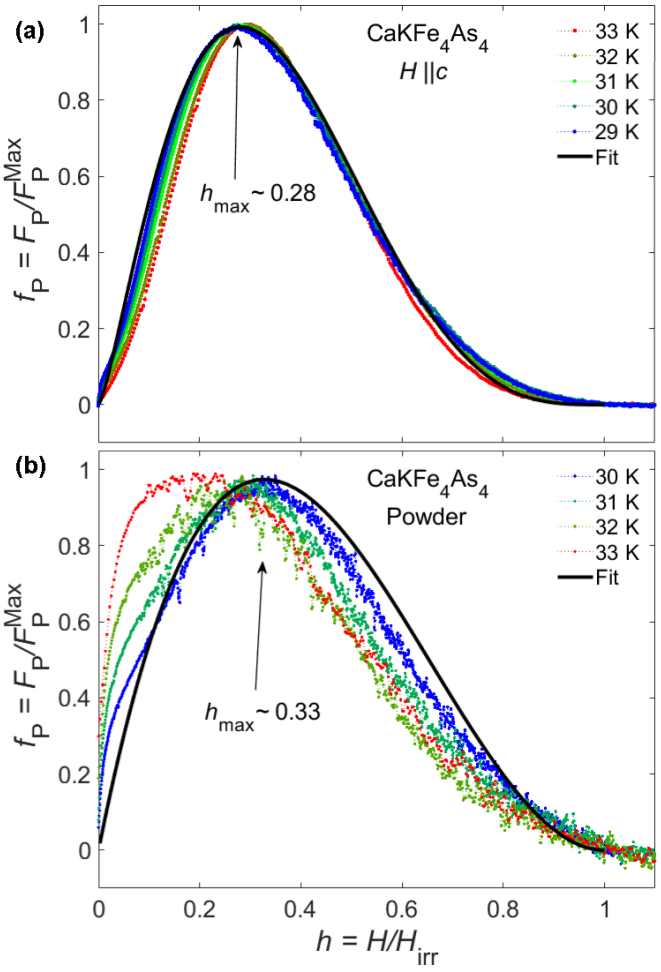

FIG. 5. The scaling density of the normalized pinning force density, f_P, for different temperatures as a function of the reduced field h based on the f_P(h) scaling function for (a) single crystal $H||c$ and (b) powder sample of $CaKFe_4As_4$. The solid line represents the fitted curve and data measured at different temperatures scaled together with the maximum reduced magnetic field at $h_{max} \sim 0.28$ for the single crystal in (a) and $h_{max} \sim 0.33$ for the powder in (b).

different temperatures should collapse into one curve, as shown in Fig. 5. The resulting scaling law is given by $f_P(h) = h^p(1-h)^q$, where F_P^{max} is the maximum pinning force density; the indices p and q are two parameters whose values depend on the origin of pinning mechanism and $h = H/H_{irr}$ is the reduced field, where the irreversibility field $\mu_0 H_{irr}$ is estimated as the magnetic field at which $J_c(H)$ reaches the background noise value, as defined in Fig. 3(a).

Figures 5(a) and 5(b) show the normalized pinning force density against the reduced magnetic field h of $CaKFe_4As_4$ estimated at different temperatures for the single crystal ($H||c$) and the powder sample. As H_{irr} exceeds the accessible magnetic field of 16 T at temperature below 27 K, only data closed to T_c are presented ($T \geqslant 29$ K). The calculated maximum pinning force density (F_P^{max}) at 30 K reaches a value of up to 9.58 GN/m^3 for the single crystal and a much reduced value of only 0.0007 GN/m^3 for the powder sample. The normalized vortex pinning force density, f_P(h), collapse onto on a single curve with a $h_{max} \sim 0.28$ for the single crystal in Fig. 5(a), indicating that a dominant pinning mechanism exists within this temperature range. For the powder sample [Fig. 5(b)], the peaks in f_P(h) are much broader, due to its granular nature, however the h_{max} value is close to that of the single crystal. The fitting parameters to the $f_P(h)$ give $p = 1.4(1)$, $q = 3.7(3)$, and $h_{max} \sim 0.28$ for the single crystal $H||c$ and $p = 1.0(1)$, $q = 2.1(1)$, and $h_{max} \sim 0.33$ for the powder sample, respectively (Fig. 5). In the Dew-Hughes model for pinning mechanism, a value of the $h_{max} \sim 0.2$ corresponds to the surface pinning for normal center of core interaction, while $h_{max} \sim 0.33$ corresponds to the point core pinning, also known as small size normal pinning [21]. Thus, $h_{max} \sim 0.28$–0.33, observed for $CaKFe_4As_4$ suggests that vortex pinning can be caused by a mixture of the surface and point core pinning of the normal centers, similar to the Fe(Se,Te) systems [49].

The obtained values of exponents p and q in $CaKFe_4As_4$ listed in Table II also support the idea that not a single model can describe the flux pinning mechanism [21] and the flux creep might have influence on the pinning force density. However, similar values of p and q have been reported for other unconventional superconductors, such as $FeTe_{0.6}Se_{0.4}$ ($h_{max} = 0.28$) and $YBa_2Cu_3O_7$ ($h_{max} = 0.33$) [49–51] (see Table II). In the 122 iron-based superconductors, the pinning mechanism depends on the doping level and dopant and h_{max} tends to increase with increasing doping level [16]. The highest J_c is achieved when $h_{max} \sim 0.40$–0.45 for the optimally-doped compounds [16]. Single crystal of $Ba_{0.6}K_{0.4}Fe_2As_2$ shows only small-size normal pinning ($h_{max} = 0.33$) [21], whereas the values obtained for $BaFe_{1.8}Co_{0.2}As_2$ single crystal [16] ($h_{max} = 0.4$, $p = 1.67$, $q = 2$) are correlated to a dense vortex pinning nanostructure, likely due to the inhomogeneous distribution of cobalt ions. A high J_c normally can be caused by a dense vortex pinning nanostructure mechanism. Violation of the scaling behavior in the underdoped and overdoped 122 iron-based superconductors implies the existence of multiple pinning sources [16]. Stoichiometric $CaKFe_4As_4$ shows superconducting behavior equivalent to an optimally-doped superconductor [16] but in the absence of inhomogeneities introduced by chemical substitution. Our scaling analysis implies that the proximity to an optimally-doping regime together with its mixed pinning mechanisms might be responsible for its high J_c.

Based on our magnetization studies, the vortex phase diagrams of $CaKFe_4As_4$ for the single crystal (when $H\|c$) and the powder sample are shown in Figs. 6(a) and 6(b). There are five different characteristic fields separating different regions of the H-T vortex phase diagram. H_{min} and H_{sp} are the magnetic field located at the valley point and the second magnetization peak, respectively, in the J_c versus H plot, as defined in Fig. 3(d). The irreversibility field H_{irr} is defined in Fig. 3(d), and H_{c1} and H_{c2} have been discussed previously in detail in Fig. 2. In the powder sample, there is no second magnetization peak. The irreversibility line, H_{irr}, is very close to H_{c2} in single crystals [Fig. 6(a)], and this is a very important feature for $CaKFe_4As_4$ to be technologically useful, as the irreversibility line demarcates the field at which vortex flow is unpinned and magnetic irreversibility sets in. On the other hand, the powder sample has H_{c2} a factor 4 larger than in single crystals and the vortex liquid state is further extended, as shown in Fig. 6(b). This suggests that grain boundaries increase

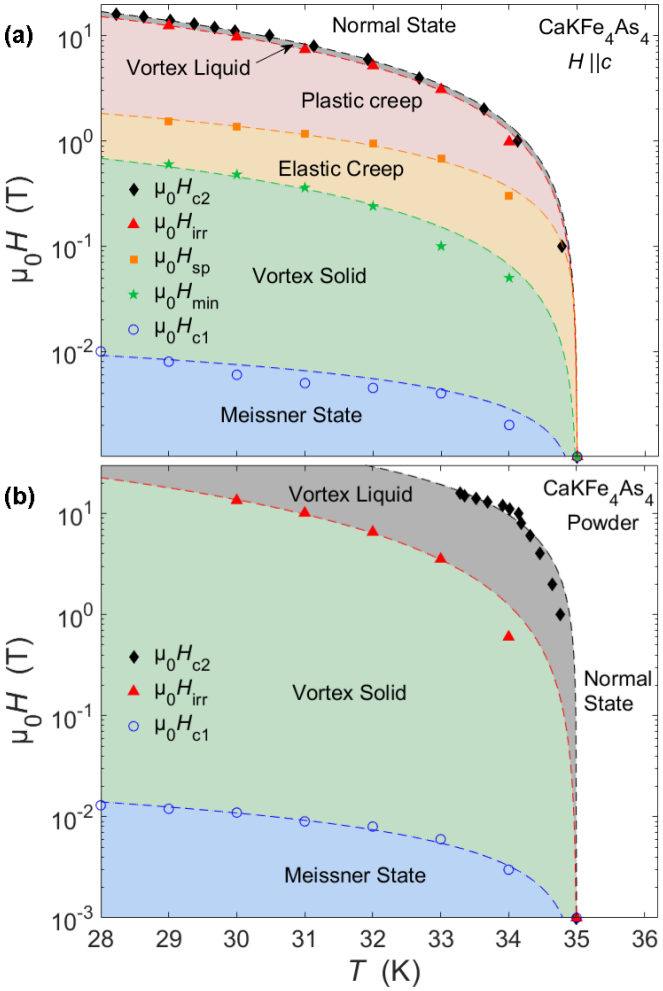

FIG. 6. The vortex phase diagram of (a) a single crystal when $H||c$ and (b) polycrystalline sample of $CaKFe_4As_4$. The different magnetic fields separating different regions in the vortex phase diagram are defined in Fig. 2 and Fig. 3. The dashed lines are fits using the empirical expression $H(T) = H(0)(1 - T/T_c)^n$.

the density of the pinning centers to give rise to larger upper critical fields, whereas the poor grain connectivity in powder is detrimental to supporting large critical currents, as they are significantly reduced.

Different regimes of vortex dynamics [52,53], marked elastic creep and plastic creep, separated by the H_{sp} line, are shown in the phase diagram in Fig. 6(a). In general, the vortex phase diagram is determined by the competition between the elastic energy of the vortex lattice, the pinning energy, and thermal energy [16]. The second magnetization peak effect is commonly associated with an order-disorder transition, which occurs at H_{min} when the pinning energy exceeds the elastic energy [24]. The motion of the vortices is governed by the elastic force in the elastic and plastic creep regions, and H_{sp} corresponds to the threshold field of the elastic-plastic crossover.

In the plastic creep region, as the magnetic field increases the vortex lattice softens and vortices are pinned more easily, resulting in an increase in J_c. As the magnetic field increases the pinning force and thermal energy affect the vortices significantly and the vortices can easily move from one pinning center to another in the vortex liquid state, which is above H_{irr}. In the case in which the pinning energy does not exceed the elastic energy in the entire field range, the SMP disappears, owing to the absence of an order-disorder transition, as in the case of the powder sample in Fig. 6(b).

The vortex phase diagram of $CaKFe_4As_4$ single crystal is very similar to that reported for the $(Ba,K)Fe_2As_2$ single crystal [34], with H_{min} having almost the same value but H_{sp} and H_{irr} being higher in the 122 compounds. The temperature dependence of the different characteristic fields in Fig. 6(a) can be fit using the empirical expression $H(T) = H(0)(1 - T/T_c)^n$, with n varying between 1.3(1) and 0.6(1). The obtained n value corresponding to the H_{min} curve is $n = 1.2(1)$, similar to values reported for other iron-based superconductors [36,54], whereas the H_{sp} and its corresponding exponent, $n = 0.83(6)$, are much smaller than those found in other systems [34,36,54]. Furthermore, the vortex phase diagram of $CaKFe_4As_4$, delimited by the temperature dependence of H_{irr}, shows a high exponent value of $n = 1.3(1)$, which cannot be understood within the framework of conventional superconductivity.

$CaKFe_4As_4$ is a stoichiometric rather clean superconductor exhibiting very high critical current values, rather unexpected, as a high density of defects is necessary to achieve such high values of J_c. However, recent STM studies find a disordered vortex lattice up to 8 T, with the vortices pinned at the locations where the superconducting order parameter is strongly suppressed due to pair breaking and the vortex core size decreases with increasing field which will give rise to very large upper critical fields [55]. The low-temperature vortex core size determined by STM is ~1.3 nm, in reasonable agreement with the value estimated from upper critical field study of ~1.9 nm, demonstrating the importance of point pinning in this material. Furthermore, the surface topography measured by STM exhibits steps on the surface due to structural defects, surface reconstruction, and small stripes, which are possible sources of surface pinning. Other types of two-dimensional surface pinning may be influenced by the anisotropic layered structure and stacking faults that may occur between Fe layers along the c axis.

The observed high J_c values are likely to be generated by intrinsic effects due to the ionic size variation that may occur in the crystallographic structure and the two-dimensional surface defects in $CaKFe_4As_4$. This structure has relevant differences compared to a 122 system, due to the absence of a glide plane and the positions of the Fe-As layers generating different Fe-As distances. The small structural defects can cause mean free path fluctuation induced pinning, which is an effective way to enhance J_c [56].

Furthermore, close to the optimal doping, as in the case of $CaKFe_4As_4$, the vortex core energy of the flux lines can be enhanced [57]. Thus, the high vortex core energy and the strength of the intrinsic depairing effect can be key factors responsible for the extremely high J_c value in this compound. Generally, the intrinsically high depairing critical density is significantly reduced due to the presence of extrinsic effects, such as weak links and grain mismatch, as for our powder sample of $CaKFe_4As_4$.

IV. CONCLUSIONS

In summary, we have investigated the critical current densities and the vortex phase diagram of an optimally-doped stoichiometric superconductor, $CaKFe_4As_4$, both in single crystal and powder form. Interestingly, we find that this material exhibits extremely large J_c values up to 10^8 A/cm^2 at low temperatures, which are some of the highest values for a iron-based superconductor. The critical current density for both in-plane and out-plane orientations has a very weak temperature dependence in the temperature range up to 25 K. The magnetization curve shows very large hysteresis loops, suggesting strong flux pinning. We detect the fish-tail effect when $H||c$, similar to other optimally-doped 122 superconducting single crystals, but this effect is missing for the $H||(ab)$ orientation and the powder sample. The flux pinning force density suggest the existence of surface and the point core pinning of the vortices in low field regime. The extremely-high critical current density of $CaKFe_4As_4$ suggests that the vortex core energy of the flux lines can be enhanced in this optimally doped superconductor and the reduced symmetry of As-Fe layers could play an important role in pinning. Furthermore, in the powder sample the critical current densities are significantly reduced due to the weak grain connectivity, as often found in other iron-based superconductors. The ultrahigh critical current densities and the vortex phase diagram of $CaKFe_4As_4$ place this stoichiometric high-T_c superconducting family as a realistic contender for practical applications.

ACKNOWLEDGMENTS

We thank A. Iyo, Y. Yoshida, and H. Eisaki for the provision of the polycrystalline sample used in this study and useful discussions. The research was funded by the Oxford Centre for Applied Superconductivity (CFAS) at Oxford University. We also acknowledge financial support of the John Fell Fund of the Oxford University. Work done at Ames Laboratory was supported by the U.S. Department of Energy, Office of Basic Energy Science, Division of Materials Sciences and Engineering. Ames Laboratory is operated for the U.S. Department of Energy by Iowa State University under Contract No. DE-AC02-07CH11358. W.R.M. was funded by the Gordon and Betty Moore Foundation's EPiQS Initiative through Grant No. GBMF4411. A.I.C. acknowledges an EPSRC Career Acceleration Fellowship (EP/I004475/1).

In accordance with the EPSRC policy framework on research data, access to the data will be made available from Ref. [58].

APPENDIX

This section provides additional information related to the superconducting parameters of $CaKFe_4As_4$ in Table I, as discussed in the main text. Furthermore, we also summarize the pinning force scaling parameters for different superconductors and $CaKFe_4As_4$ in Table II. Structural characterization of the single crystal and powder sample are shown in Figs. 7 and 8, respectively. Magnetization measurements on other single crystals are presented in Fig. 9.

TABLE I. The extracted superconducting parameters: the transition temperature T_c, the slope of the upper critical field close to T_c, the upper critical field H_{c2} extrapolated at zero temperature, the lower critical field H_{c1}^* and the critical current density J_c (extrapolated at zero magnetic field) of the single crystal (S1) presented in the main text and the powder sample of $CaKFe_4As_4$. Results for two additional single crystals, S2 and S4, are also provided.

Parameters	Single crystal		Powder
	$H\|\|(ab)$	$H\|\|c$	
T_c(K)	35.0(1)	35.1(2)	34.9(2)
μ_0d H_{c2}/dT(T/K)	5.7	2.6	10.1
$\mu_0 H_{c2}(0)$(T)	135	62	241
$\mu_0 H_{c1}^*$(2 K)(T)	0.1114	0.0220	0.0549
J_c(A/cm^2) (5 K)(S1)	$1.9(2) \times 10^8$	$0.9(2) \times 10^7$	4.4×10^3
J_c(A/cm^2) (5 K) (S2)	$0.8(2) \times 10^8$	$0.5(2) \times 10^7$	–
J_c(A/cm^2) (5 K) (S4)	–	$0.4(2) \times 10^7$	–

TABLE II. Summary of the pinning force scaling parameters p, q, and h_{max} for different superconductors.

Single crystal	p	q	$h_{max} = p/(p+q)$	Peak position
$CaKFe_4As_4$	1.4(1)	3.7(3)	0.28	0.28
$Ba_{0.6}K_{0.4}Fe_2As_2$ [34]	1	2	0.33	0.33
$Ba_{0.68}K_{0.32}Fe_2As_2$ [59]				0.43
$BaFe_{1.8}Co_{0.2}As_2$ [60]	1.67	2	0.45	0.45
$BaFe_{1.85}Co_{0.15}As_2$ [59]				0.37
$BaFe_{1.29}Ru_{0.71}As_2$ [61]	1.95	2.5	0.44	0.45
$BaFe_{1.91}Ni_{0.09}As_2$ [59]				0.32
$FeTe_{0.7}Se_{0.3}$				0.27
$FeTe_{0.6}Se_{0.4}$ [49]	1.54	3.8	0.28	0.28
$K_xFe_{2-y}Se_2$ [62]	0.86	1.83	0.32	0.33
$YBa_2Cu_3O_7$ [50]	2	4	0.33	0.33
$NdBa_2Cu_3O_{7-d}$ [63]	1.48	2.23	0.45	0.45
$Sm_{0.5}Eu_{0.5}Ba_2Cu_3O_7$ [51]	2.08	3.56	0.37	0.37

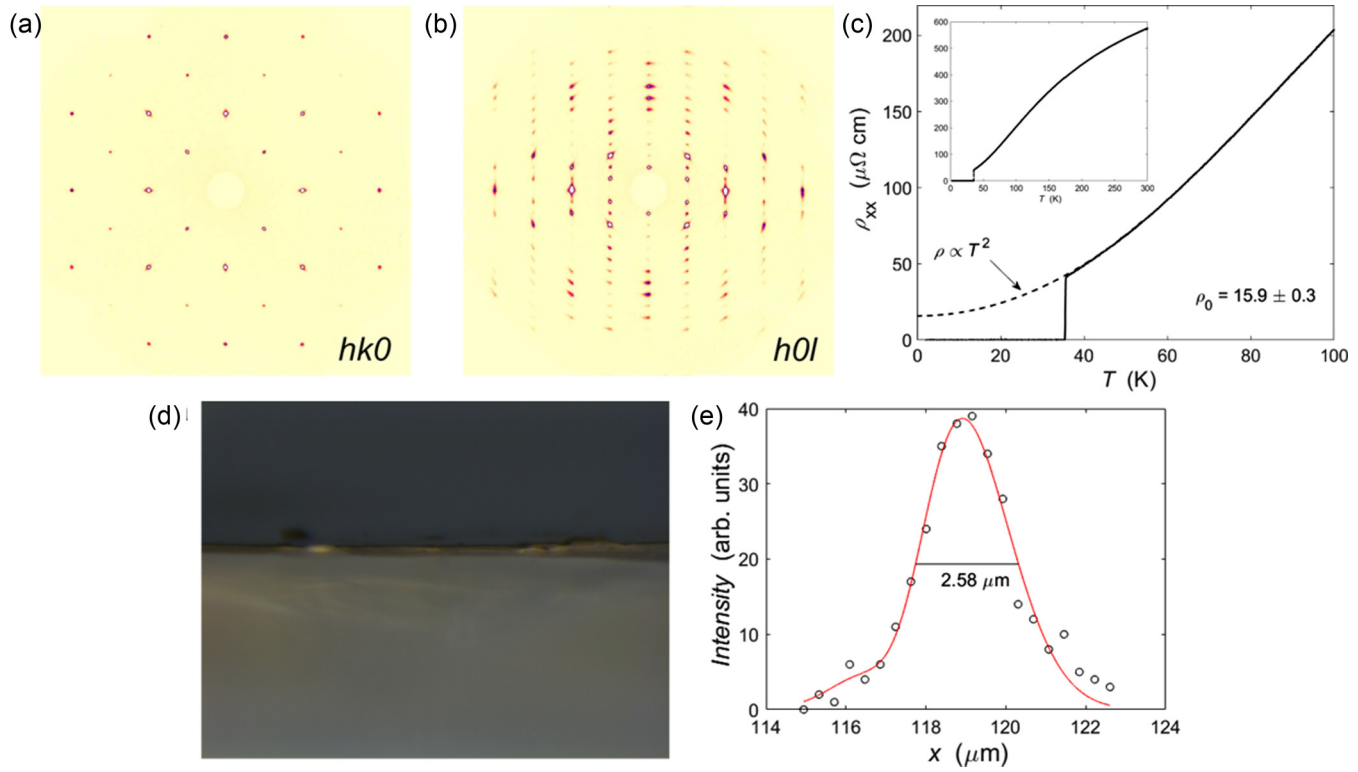

FIG. 7. X-ray diffraction pattern of (a) the ($hk0$) and (b) the ($h0l$) plane for a single crystal from the same batch like the measured crystal. (c) Resistivity data showing the very high quality of our single crystals giving an extrapolated low-temperature residual resistivity of $\rho_0 \sim 15.9(3)$ $\mu\Omega$ cm. The residual resistivity ratio, RRR(defined as $\rho_{300\,\mathrm{K}}/\rho_{36\,\mathrm{K}}$) is ∼14, in agreement with previous reports [10], and together with the small superconducting transition width (ΔT_c) of 0.3 K, reflect the very high quality of our single crystal. (d) Optical image of the single crystal used in the magnetization studies. (e) The estimation of the sample thickness from (d) by fitting to a gaussian distribution of the intensity.

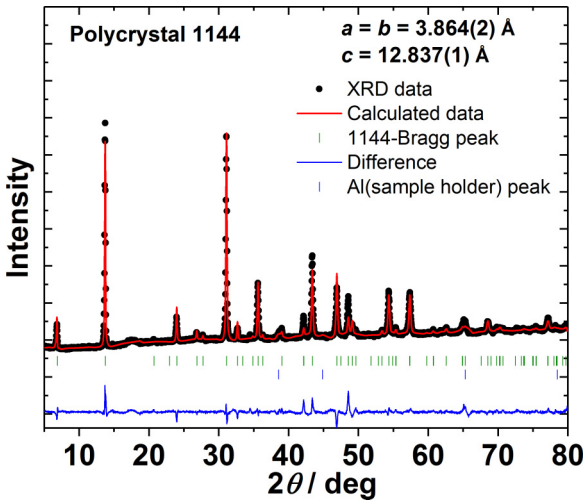

FIG. 8. Powder x-ray diffraction patterns (XRD) and Rietveld refinement of the polycrystalline sample of $CaKFe_4As_4$ used in this study. The x-ray data show that this is a single phase compound with the extracted lattice parameters closed to those reported for the single crystal ($a = 3.8659$ Å, $c = 12.884$ Å [10]).

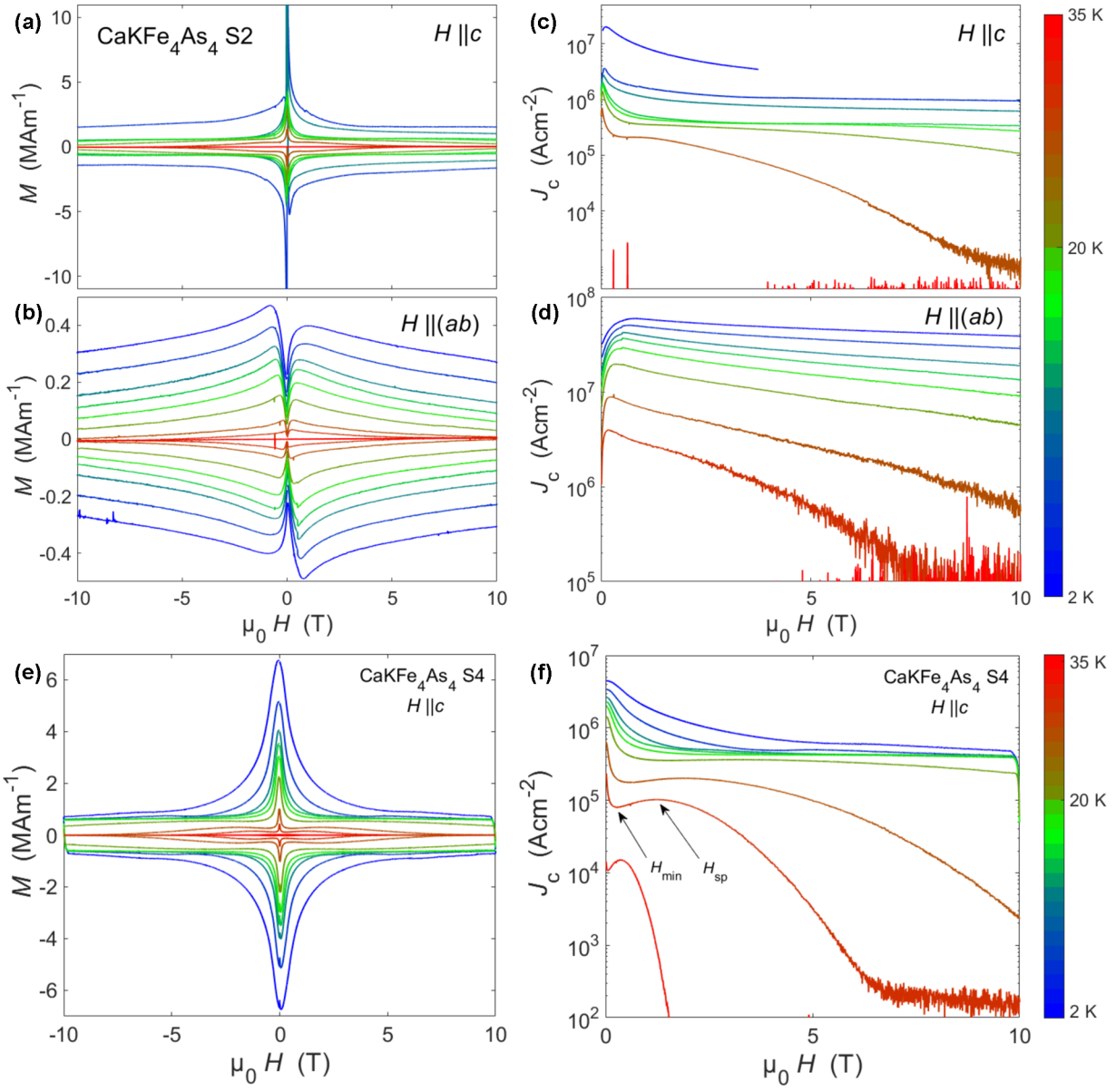

FIG. 9. (a), (b) Magnetization and (c), (d) critical current density for different single crystals, S2 (with thickness around 12 μm) measured with $H\|c$ and $H\|(ab)$, respectively. (e) Magnetization and (f) critical current density for the single crystal S4 (with thickness around 15 μm) measured with $H\|c$.

[1] Y. Kamihara, T. Watanabe, M. Hirano, and H. Hosono, Iron-based layered superconductor $LaO_{1-x}F_xFeAs$ with $T_c = 26$ K, J. Am. Chem. Soc. **130**, 3296 (2008).

[2] H. Hosono, K. Tanabe, E. Takayama-Muromachi, H. Kageyama, S. Yamanaka, H. Kumakura, M. Nohara, H. Hiramatsu, and S. Fujitsu, Exploration of new superconductors and functional materials, and fabrication of superconducting tapes and wires of iron pnictides, Sci. Technol. Adv. Mater. **16**, 033503 (2015).

[3] Z. A. Ren, G. C. Che, X. L. Dong, J. Yang, W. Lu, W. Yi, X. L. Shen, Z. C. Li, L. L. Sun, F. Zhou, and Z. X. Zhao, Superconductivity and phase diagram in iron-based arsenic-oxides ReFeAsO (Re = rare-earth metal) without fluorine doping, Europhy. Lett. **83**, 17002 (2008).

[4] S. J. Singh, J. Shimoyama, A. Yamamoto, H. Ogino, and K. Kishio, Transition temperature and upper critical field in $SmFeAsO_{1-x}F_x$ synthesized at low heating temperatures, IEEE Trans. Appl. Supercond. **23**, 7300605 (2013).

[5] J. Jaroszynski, F. Hunte, L. Balicas, Youn-jung Jo, I. Raičević, A. Gurevich, D. C. Larbalestier, F. F. Balakirev, L. Fang, P. Cheng, Y. Jia, and H. H. Wen, Upper critical fields and thermally-activated transport of $NdFeAsO_{0.7}F_{0.3}$ single crystal, Phys. Rev. B **78**, 174523 (2008).

[6] J. Jaroszynski, S. C. Riggs, F. Hunte, A. Gurevich, D. C. Larbalestier, G. S. Boebinger, F. F. Balakirev, A. Migliori, Z. A. Ren, W. Lu, J. Yang, X. L. Shen, X. L. Dong, Z. X. Zhao, R. Jin, A. S. Sefat, M. A. McGuire, B. C. Sales, D. K. Christen, and D. Mandrus, Comparative high-field magnetotransport of the oxypnictide superconductors RFeAsO$_{1-x}$F$_x$ (R = La, Nd) and SmFeAsO$_{1-\delta}$, Phys. Rev. B **78**, 064511 (2008).

[7] Y. Ma, Progress in wire fabrication of iron-based superconductors, Supercond. Sci. Technol. **25**, 113001 (2012).

[8] J. Shimoyama, Potentials of iron-based superconductors for practical future materials, Supercond. Sci. Technol. **27**, 044002 (2014).

[9] A. Iyo, K. Kawashima, T. Kinjo, T. Nishio, S. Ishida, H. Fujihisa, Y. Gotoh, K. Kihou, H. Eisaki, and Y. Yoshida, New-structure-type fe-based superconductors: CaAFe$_4$As$_4$ (A = K, Rb, Cs) and SrAFe$_4$As$_4$ (A = Rb, Cs), J. Am. Chem. Soc. **138**, 3410 (2016).

[10] W. R. Meier, T. Kong, U. S. Kaluarachchi, V. Taufour, N. H. Jo, G. Drachuck, A. E. Böhmer, S. M. Saunders, A. Sapkota, A. Kreyssig, M. A. Tanatar, R. Prozorov, A. I. Goldman, F. F. Balakirev, A. Gurevich, S. L. Bud'ko, and P. C. Canfield, Anisotropic thermodynamic and transport properties of single crystalline CaKFe$_4$As$_4$, Phys. Rev. B **94**, 064501 (2016).

[11] M. Rotter, M. Tegel, and D. Johrendt, Superconductivity at 38 K in the Iron Arsenide (Ba$_{1-x}$K$_x$)Fe$_2$As$_2$, Phys. Rev. Lett. **101**, 107006 (2008).

[12] D. Mou, T. Kong, W. R. Meier, F. Lochner, L.-L. Wang, Q. Lin, Y. Wu, S. L. Bud'ko, I. Eremin, D. D. Johnson, P. C. Canfield, and A. Kaminski, Enhancement of the Superconducting Gap by Nesting in CaKFe$_4$As$_4$: A New High Temperature Superconductor, Phys. Rev. Lett. **117**, 277001 (2016).

[13] W. R. Meier, Q.-P. Ding, A. Kreyssig, S. L. Bud'ko, A. Sapkota, K. Kothapalli, V. Borisov, R. Valentí, C. D. Batista, P. P. Orth, R. M. Fernandes, A. I. Goldman, Y. Furukawa, A. E. Böhmer, and P. C. Canfield, Hedgehog spin-vortex crystal stabilized in a hole-doped iron-based superconductor, npj Quantum Materials, **3**, 5 (2018).

[14] D. C. Johnston, The puzzle of high temperature superconductivity in layered iron pnictides and chalcogenides, Adv. Phys. **59**, 803 (2010).

[15] P. J. Hirschfeld, Using gap symmetry and structure to reveal the pairing mechanism in Fe-based superconductors, C. R. Phys. **17**, 197 (2016).

[16] S. Ishida, D. Song, H. Ogino, A. Iyo, H. Eisaki, M. Nakajima, Jun-ichi Shimoyama, and M. Eisterer, Doping-dependent critical current properties in K, Co, and P-doped BaFe$_2$As$_2$ single crystals, Phys. Rev. B **95**, 014517 (2017).

[17] G. Blatter, M. V. FeigelMan, V. B. Geshkenbein, A. I. Larkin, and V. M. Vinokur, Vortices in high-temperature superconductors, Rev. Mod. Phys. **66**, 1125 (1994).

[18] M. V. Feigelman, V. B. Geshkenbein, A. I. Larkin, and V. M. Vinokur, Theory of Collective Flux Creep, Phys. Rev. Lett. **63**, 2303 (1989).

[19] W. R. Meier, T. Kong, S. L. Bud'ko, and P. C. Canfield, Optimization of the crystal growth of the superconductor CaKFe$_4$As$_4$ from solution in the FeAs−CaFe$_2$As$_2$−KFe$_2$As$_2$ system, Phys. Rev. Mater. **1**, 013401 (2017).

[20] P. C. Bean, Magnetization of high-field superconductors, Rev. Mod. Phys. **36**, 31 (1985).

[21] D. D. Dew-Hughes, Flux pinning mechanisms in type II superconductors, Philos. Mag. **30**, 293 (1974).

[22] D. X. Chen, E. Pardo, and A. Sanchez, Demagnetizing factors of rectangular prisms and ellipsoids, IEEE Trans. Magnet. **38**, 1742 (2002).

[23] M. Naito, A. Matsuda, K. Kitazawa, S. Kambe, I. Tanaka, and H. Kojima, Temperature dependence of anisotropic lower critical fields in La$_{1-x}$Sr$_x$CuO$_4$, Phys. Rev. B **41**, 4823 (1990).

[24] E. H. Brandt, Irreversible magnetization of pin-free type-II superconductors, Phys. Rev. B **60**, 11939 (1999).

[25] S. J. Singh, J. ichi Shimoyama, A. Yamamoto, H. Ogino, and K. Kishio, Significant enhancement of the intergrain coupling in lightly F-doped SmFeAsO superconductors, Supercond. Sci. Technol. **26**, 065006 (2013).

[26] P. K. Biswas, A. Iyo, Y. Yoshida, H. Eisaki, K. Kawashima, and A. D. Hillier, Signature of multigap nodeless superconductivity in CaKFe$_4$As$_4$, Phys. Rev. B **95**, 140505 (2017).

[27] N. R. Werthamer, E. Helfand, and P. C. Hohenberg, Temperature and purity dependence of the superconducting critical field, H_{c2}. III. electron spin and spin-orbit effects, Phys. Rev. **147**, 295 (1966).

[28] M. Bristow (unpublished).

[29] Z. S. Wang, H. Q. Luo, C. Ren, and H. H. Wen, Upper critical field, anisotropy, and superconducting properties of Ba$_{1-x}$K$_x$Fe$_2$As$_2$ single crystals, Phys. Rev. B **78**, 140501 (2008).

[30] A. M. Clogston, Upper Limit for the Critical Field in Hard Superconductors, Phys. Rev. Lett. **9**, 266 (1962).

[31] K. Cho, A. Fente, S. Teknowijoyo, M. A. Tanatar, K. R. Joshi, N. M. Nusran, T. Kong, W. R. Meier, U. Kaluarachchi, I. Guillamón, H. Suderow, S. L. Bud'ko, P. C. Canfield, and R. Prozorov, Nodeless multiband superconductivity in stoichiometric single-crystalline CaKFe$_4$As$_4$, Phys. Rev. B **95**, 100502 (2017).

[32] R. Khasanov, W. R. Meier, Y. Wu, D. Mou, S. L. Bud'ko, I. Eremin, H. Luetkens, A. Kaminski, P. C. Canfield, and A. Amato, In-plane magnetic penetration depth of superconducting CaKFe$_4$As$_4$, Phys. Rev. B **97**, 140503(R) (2018).

[33] L. Fang, Y. Jia, V. Mishra, C. Chaparro, V. K. Vlasko-Vlasov, A. E. Koshelev, U. Welp, G. W. Crabtree, S. Zhu, N. D. Zhigadlo, S. Katrych, J. Karpinski, and W. K. Kwok, Huge critical current density and tailored superconducting anisotropy in SmFeAsO$_{0.8}$F$_{0.15}$ by low-density columnar-defect incorporation, Nat. Commun. **4**, 2655 (2013).

[34] H. Yang, H. Luo, Z. Wang, and H.-H. Wen, Fishtail effect and the vortex phase diagram of single crystal Ba$_{0.6}$K$_{0.4}$Fe$_2$As$_2$, Appl. Phys. Lett. **93**, 142506 (2008).

[35] T. Taen, Y. Tsuchiya, Y. Nakajima, and T. Tamegai, Superconductivity at $T_c \sim 14$ K in single-crystalline FeTe$_{0.61}$Se$_{0.39}$, Phys. Rev. B **80**, 092502 (2009).

[36] A. K. Pramanik, L. Harnagea, C. Nacke, A. U. B. Wolter, S. Wurmehl, V. Kataev, and B. Büchner, Fishtail effect and vortex dynamics in LiFeAs single crystals, Phys. Rev. B **83**, 094502 (2011).

[37] M. Eisterer, Magnetic properties and critical currents of MgB$_2$, Supercond. Sci. Technol. **20**, R47 (2007).

[38] J. Moore and G. K. Perkins, Critical fields and critical currents in MgB$_2$, Supercond. Sci. Technol. **16**, 176 (2003).

[39] C. Buzea and T. Yamashita, Review of the superconducting properties of MgB$_2$, Supercond. Sci. Technol. **14**, R115 (2001).

[40] R. W. Heussner, J. D. Marquardt, P. J. Lee, and D. C. Larbalestier, Increased critical current density in Nb-Ti wires having Nb artificial pinning centers, Appl. Phys. Lett. **70**, 901 (1997).

[41] T. Tamegai, T. Taen, H. Yagyuda, Y. Tsuchiya, S. Mohan, T. Taniguchi, Y. Nakajima, S. Okayasu, M. Sasase, H. Kitamura, T. Murakami, T. Kambara, and Y. Kanai, Effects of particle irradiations on vortex states in iron-based superconductors, Supercond. Sci. Technol. **25**, 084008 (2012).

[42] G. P. Mikitik and E. H. Brandt, Critical state in thin anisotropic superconductors of arbitrary shape, Phys. Rev. B **62**, 6800 (2000).

[43] U. Welp, W. K. Kwok, G. W. Crabtree, K. G. Vandervoort, and J. Z. Liu, Magnetization hysteresis and flux pinning in twinned and untwinned $YBa_2Cu_3O_{7-x}$ single crystals, Appl. Phys. Lett. **57**, 84 (1990).

[44] Y. Yeshurun, N. Bontemps, L. Burlachkov, and A. Kapitulnik, Dynamic characteristics of the anomalous second peak in the magnetization curves of Bi-Sr-Ca-Cu-O, Phys. Rev. B **49**, 1548 (1994).

[45] R. Lortz, N. Musolino, Y. Wang, A. Junod, and N. Toyota, Origin of the magnetization peak effect in the Nb_3Sn superconductor, Phys. Rev. B **75**, 094503 (2007).

[46] M. Pissas, S. Lee, A. Yamamoto, and S. Tajima, Peak Effect in Single Crystal MgB_2 Superconductor for $H||c$-Axis, Phys. Rev. Lett. **89**, 097002 (2002).

[47] Y. B. Kim, C. F. Hempstead, and A. R. Strnad, Flux creep in hard superconductors, Phys. Rev. **131**, 2486 (1963).

[48] P. W. Anderson and Y. B. Kim, Hard superconductivity: Theory of the motion of Abrikosov flux lines, Rev. Mod. Phys. **36**, 39 (1964).

[49] C. S. Yadav and P. L. Paulose, The flux pinning force and vortex phase diagram of single crystal $FeTe_{0.60}Se_{0.40}$, Solid State Commun. **151**, 216 (2011).

[50] L. Klein, E. R. Yacoby, Y. Yeshurun, A. Erb, G. Müller-Vogt, V. Breit, and H. Wühl, Peak effect and scaling of irreversible properties in untwinned Y-Ba-Cu-O crystals, Phys. Rev. B **49**, 4403 (1994).

[51] H. Wen and Z. X. Zhao, Fishtail effect and small size normal core pinning in melt-textured-growth YBa_2Cu_3O bulks, Appl. Phys. Lett. **68**, 856 (1996).

[52] R. Prozorov, N. Ni, M. A. Tanatar, V. G. Kogan, R. T. Gordon, C. Martin, E. C. Blomberg, P. Prommapan, J. Q. Yan, S. L. Bud'ko, and P. C. Canfield, Vortex phase diagram of $Ba(Fe_{0.93}Co_{0.07})_2as_2$ single crystals, Phys. Rev. B **78**, 224506 (2008).

[53] S. Salem-Sugui, L. Ghivelder, A. D. Alvarenga, L. F. Cohen, K. A. Yates, K. Morrison, J. L. Pimentel, H. Luo, Z. Wang, and H.-H. Wen, Flux dynamics associated with the second magnetization peak in the iron pnictide $Ba_{1-x}K_xFe_2As_2$, Phys. Rev. B **82**, 054513 (2010).

[54] P. Das, A. D. Thakur, A. K. Yadav, C. V. Tomy, M. R. Lees, G. Balakrishnan, S. Ramakrishnan, and A. K. Grover, Magnetization hysteresis and time decay measurements in $FeSe_{0.50}Te_{0.50}$: Evidence for fluctuation in mean free path induced pinning, Phys. Rev. B **84**, 214526 (2011).

[55] A. Fente, W. R. Meier, T. Kong, V. G. Kogan, S. L. Bud'ko, P. C. Canfield, I. Guillamón, and H. Suderow, Influence of multiband sign-changing superconductivity on vortex cores and vortex pinning in stoichiometric high-T_c $CaKFe_4As_4$, Phys. Rev. B **97**, 134501 (2018).

[56] R. Griessen, Wen Hai-hu, A. J. J. van Dalen, B. Dam, J. Rector, H. G. Schnack, S. Libbrecht, E. Osquiguil, and Y. Bruynseraede, Evidence for Mean Free Path Fluctuation Induced Pinning in $YBa_2Cu_3O_7$ and $YBa_2Cu_4O_8$ Films, Phys. Rev. Lett. **72**, 1910 (1994).

[57] C. Putzke, P. Walmsley, J. D. Fletcher, L. Malone, D. Vignolles, C. Proust, S. Badoux, P. See, H. E. Beere, D. Ritchie, S. Kasahara, Y. Mizukami, T. Shibauchi, Y. Matsuda, and A. Carrington, Anomalous critical fields in quantum critical superconductors, Nat. Commun. **5**, 5679 (2014).

[58] https://doi.org/10.5287/bodleian:dmZ8wEOk5.

[59] D. L. Sun, Y. Liu, and C. T. Lin, Comparative study of upper critical field H_{c2} and second magnetization peak H_{sp} in hole- and electron-doped $BaFe_2As_2$ superconductor, Phys. Rev. B **80**, 144515 (2009).

[60] A. Yamamoto, J. Jaroszynski, C. Tarantini, L. Balicas, J. Jiang, A. Gurevich, D. C. Larbalestier, R. Jin, A. S. Sefat, M. A. McGuire, B. C. Sales, D. K. Christen, and D. Mandrus, Small anisotropy, weak thermal fluctuations, and high field superconductivity in Co-doped iron pnictide $Ba(Fe_{1-x}Co_x)_2As_2$, Appl. Phys. Lett. **94**, 062511 (2009).

[61] S. Sharma, K. Vinod, C. S. Sundar, and A. Bharathi, Critical current density and magnetic phase diagrams of $Ba(Fe,Ru)_2As_2$ single crystals, Supercond. Sci. Technol. **26**, 015009 (2013).

[62] H. Lei and C. Petrovic, Giant increase in critical current density of $K_xFe_{2-y}Se_2$ single crystals, Phys. Rev. B **84**, 212502 (2011).

[63] M. R. Koblischka, T. Higuchi, S. I. Yoo, and M. Murakami, Scaling of pinning forces in $NdBa_2Cu_3O_{7-d}$ superconductors, J. Appl. Phys. **85**, 3241 (1999).